Electrode Spacing and Collector Radius Effects on the Thrust-to-Power Ratio of a Low-Cost Wire-to-Ring EHD Thruster: An Accessible Platform for Quantitative Propulsion Analysis

Said Zeki Gökmen[1]

[1] Independent Researcher, Oslo, Norway
Correspondence: saidzekigokmen34@gmail.com

Abstract

Electrode geometry governs the efficiency with which an electrohydrodynamic (EHD) thruster converts electrical energy into directed momentum, yet the independent contributions of emitter-to-collector spacing and collector radius remain incompletely characterized in simple wire-to-ring configurations. This study quantifies both using a low-cost apparatus suitable for instructional use. Two one-factor-at-a-time sweeps were conducted under unipolar positive corona at an estimated interelectrode potential of 37.4 kV: collector radius from 0.5 to 3.0 cm at a fixed spacing of 4.0 cm, and axial spacing from 4.0 to 8.0 cm at a fixed radius of 2.5 cm. Centerline exhaust velocity was recorded with a vane anemometer, converted into momentum-based thrust estimates through a steady control-volume analysis, and normalized by the nominal battery-side system input power (34.632 W). The measurements were compared against a geometry-adapted model combining Mott-Gurney space-charge-limited current density with a spherical-sector representation of the discharge. The measured system thrust-to-power ratio increased from 1.47 ± 0.24 to 142.98 ± 8.86 mN kW^{-1} with collector radius and decreased from 84.68 ± 1.83 to 0.44 ± 0.47 mN kW^{-1} with spacing, following Rc4.21 and d-6.94. The model reproduced both trend directions but predicted far weaker scaling (Rc1.94 and d-1.91). Its over-prediction narrowed with increasing radius and widened with increasing spacing, indicating a geometry-dependent discrepancy rather than a fixed calibration offset and suggesting a possible role for the unmeasured discharge current.

Keywords: electrohydrodynamic thruster; ionic wind; corona discharge; electrode geometry; thrust-to-power ratio; space-charge-limited current; engineering education

Highlights:

- Collector radius and electrode spacing varied independently in a wire-to-ring EHD thruster
- Measured thrust-to-power ratio scaled as $R_c^{4.21}$ and $d^{-6.94}$ over the tested ranges
- An idealized space-charge-limited model captured trend direction but not its strength
- Model over-prediction was geometry-dependent, narrowing with increasing radius and widening with increasing spacing.
- Apparatus enables quantitative teaching of propulsion, uncertainty, and model limits

1. Introduction

Space exploration has long been driven by the continuous improvement of propulsion technologies. Chemical propulsion provides high thrust, but its comparatively limited specific impulse makes propellant requirements increasingly restrictive for long-duration and high acceleration missions. (SPL MIT, n.d.). Electric propulsion offers an alternative by using electrical energy to accelerate propellant through electrostatic or electromagnetic mechanisms. (NASA, n.d.).

Among these technologies, ion thrusters represent a particularly promising variant. By ionizing a neutral propellant, stripping electrons to form positively charged ions, these systems accelerate the resulting plasma through an electric field established between carefully shaped electrodes to produce a high-velocity ion beam (NASA, 2015). Consequently, they deliver exceptionally high specific impulse ranging from 1,500 to 10,000 seconds and exhaust velocities of 20 to 50 km/s. This drastically outpaces chemical propulsion, which rarely exceeds a specific impulse of 450 to 500 seconds, making ion systems ideal for deep-space missions where propellant mass is tightly constrained (NASA, 2024).

Despite these advantages, many in-space ion propulsion systems produce relatively low thrust for their electrical power requirements (Gadisa & Bang, 2023). Electrohydrodynamic (EHD) thrusters are a related class of ion-driven electric propulsion devices and provide an experimentally accessible atmospheric platform for studying electrode-geometry effects, although their thrust mechanism differs from that of in-space ion thrusters. In atmospheric EHD thrusters, electrode geometry is an important performance parameter because the emitter-to-collector spacing and collector shape influence the electric field, ion transport, and aerodynamic interaction with the induced flow (Belan et al., 2021; Kahol et al., 2023). Analytical EHD models show that electrode separation influences electric-field strength, charge transport, and the resulting momentum transfer, while broader reviews identify electrode geometry as an important design parameter across EHD systems (Vaddi et al., 2020; Iranshahi et al., 2024).

Yet, the combined parametric influence of these variables remains less explored in highly simplified point-to-ring configurations. Some existing studies, such as Gu et al. (2023), focus on applied-voltage polarity, electrode curvature, and the resulting corona current and thrust rather than independently varying collector radius and axial electrode spacing. Others, including Burghard et al. (2023), center on electrode-number ratios and their effects on thrust, current draw, and thrust efficiency rather than separately varying collector radius and emitter-to-collector spacing. The present study therefore examines a complementary geometric question by varying both axial spacing and collector radius. This gap prompts the central question of this investigation: *How do electrode spacing and collector electrode radius affect the thrust-to-power ratio of a model atmospheric EHD thruster, and to what extent do the measured trends agree with an idealized analytical model?*

Belan et al. (2021) investigated how collector shape affects atmospheric EHD thruster performance by testing airfoil-shaped collectors of fixed chord and different profiles, finding that the NACA 0010 profile provided particularly strong thrust-to-power performance at larger spacings. This supports that collector geometry significantly modulates performance through both electric field shaping and aerodynamic drag. Following this, Belan et al. (2022) explored emitter density within an array, finding an optimum 2:1 collector-to-emitter spacing ratio, while further increases in emitter density degraded performance, plausibly because of electrostatic shielding. Furthermore, studies on wire-to-airfoil configurations highlight that increasing the gap distance between electrodes actively enhances the thrust-to-power ratio, though it simultaneously penalizes absolute thrust density (Kahol et al., 2023).

More recent studies have pushed performance boundaries through complex collector architectures. Terenzi et al. (2025) proposed major thrust density gains using grid-based collectors, noting that performance hinges on balancing electrostatic acceleration against aerodynamic

penalties. Similarly, Hou et al. (2025) tested a sawtooth multi-ring emitter paired with concentric ring collectors, achieving a maximum thrust per unit length of 164 mN/m at 40 kV with a 60 mm gap. These studies demonstrate that geometry is a key factor in atmospheric EHD thruster performance and that structured, multi-element geometries can substantially improve performance over simpler designs. However, they largely focus on complex multi-unit arrays or detailed flow modeling rather than providing a clean, single-variable comparison of electrode spacing and collector radius in a fundamental wire-to-ring configuration.

The educational utility of EHD and ionic-wind systems has also been recognized in physics-teaching literature. Hart and Massey (1981) introduced EHD classroom demonstrations, showing how electrohydrodynamic effects can be made directly observable to students. Przeniczny (1972) similarly showed electric-wind experiments to stimulate student interest in field-driven propulsion. Furthermore, Kuhnen et al. (2007) investigated the forces acting on asymmetric capacitors and used high-voltage levitation demonstrations with undergraduate and graduate physics students to explain the effect through ionic wind rather than speculative antigravity mechanisms. Later, Cattani et al. (2015) described the construction of high-voltage lifter devices and presented a simplified theoretical model for physics and engineering students, explaining the levitation force through corona discharge, ion acceleration, and momentum transfer to neutral air.

However, while these educational studies demonstrate the physical mechanisms of ionization, electrostatics, ionic wind, and momentum transfer, they generally emphasize demonstration, device construction, or simplified physical explanation. What remains less common is an accessible, controlled experiment that transitions EHD from a visual demonstration into a quantitative teaching platform. The aforementioned educational studies do not systematically isolate collector radius and electrode spacing to calculate thrust-to-power ratio or treat the mismatch between an ideal analytical model and real atmospheric measurements as a central learning objective.

This study directly addresses these scientific and educational gaps. By using a simplified wire-to-ring model thruster where emitter geometry and the electrical supply configuration are held constant, electrode spacing and collector radius are systematically varied. Exhaust velocity is measured as a neutral-flow proxy for thrust, and the resulting estimates are divided by electrical input power to evaluate each configuration based on its thrust-to-power ratio. The experimental data are then compared against an analytical EHD thrust model grounded in space-charge-limited current and Coulomb body-force density. This work builds directly on a prior study that identified a strong qualitative dependence of thrust-to-power ratio on electrode geometry (Gökmen, 2025). The present investigation extends that work using a system-level power definition and an explicitly idealized analytical comparison model.

The primary objectives of this research are therefore to: (1) quantitatively determine the isolated effects of emitter-to-collector spacing and collector radius on the thrust-to-power ratio of a simplified wire-to-ring EHD thruster under atmospheric conditions; (2) evaluate the extent to which these experimental performance trends align with or depart from idealized analytical EHD models based on space-charge-limited current, specifically clarifying the role of effective discharge current and atmospheric losses; and (3) establish an accessible, low-budget educational platform that enables engineering and physics students to investigate propulsion trade-offs, electrostatic field constraints, measurement uncertainty, and the inherent limitations of idealized analytical models in introductory aerospace and engineering contexts.

The remainder of this paper is organized as follows: Section 2 presents the theoretical background and analytical model; Section 3 describes the experimental methodology and data-processing approach; Section 4 presents and discusses the experimental and theoretical results; and Section 5 summarizes the main conclusions.

2. Theoretical Background

2.1. Electrohydrodynamic Body Force and Ion Drift

In an atmospheric electrohydrodynamic (EHD) thruster operating under unipolar corona discharge, propulsive force arises through momentum transfer from electrostatically accelerated ions to ambient neutral air molecules (Castellanos, 1998). As illustrated in Figure 1, ions are generated within a thin, high-field ionization layer surrounding the emitter tip of radius a. These ions drift along electric field lines toward the collector ring of inner radius R_c.

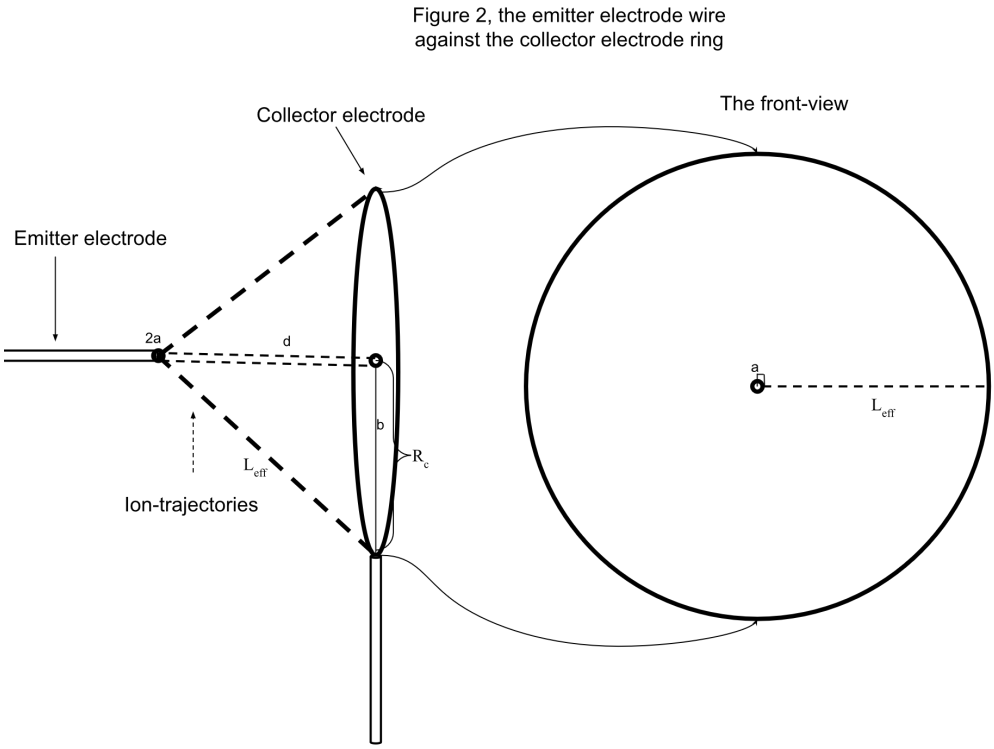

Figure 1. Cross-sectional and front-view geometry of the wire-to-ring electrohydrodynamic (EHD) thruster under unipolar corona operation. a is the thin emitter electrode of radius, R_c is the circular collector ring of inner radius, d is the axial separation distance, and L_{eff} is the geometry-specific effective-distance approximation used in this study.

During this drift phase, the ions experience frequent collisions with neutral air molecules, transferring kinetic energy and momentum to the bulk gas to produce an induced airflow known as an ionic wind (Raizer, 1991). Although only a small fraction of the gas is ionized, the electric body force depends on the space-charge density, while the resulting bulk airflow consists predominantly of neutral gas accelerated through ion-neutral momentum transfer (Monrolin et al., 2018; Vaddi et al., 2020).

The ion motion is driven by the Coulomb force $\vec{F_C} = q\vec{E}$, which manifests as a volumetric continuum body-force density $\vec{f}$ acting on the medium (Castellanos, 1998):

$$f = \rho_e \, E \qquad \text{Eqn (1)}$$

where ρ_e is the space-charge density and E is the electric field magnitude. Under a drift-dominated approximation, where ion diffusion and bulk-flow convection are neglected relative to electric-field-driven ion motion, the current density can be approximated as $J \approx \rho_e \, \mu \, E$

(Vaddi et al., 2020). Substituting this relationship allows the volumetric body-force density to be expressed directly in terms of current density:

$$f \approx \frac{J}{\mu} \qquad \text{Eqn (2)}$$

Integrating this body-force density over the entire volume V of the ion drift region yields the total electrostatic thrust F generated between electrodes:

$$F = \int_V f \, dV = \int_V \frac{J}{\mu} \, dV \qquad \text{Eqn (3)}$$

Under ideal steady unipolar conditions, with negligible charge loss within the drift region and approximately uniform ion mobility, conservation of charge requires the total current to remain constant through the drift region (Sigmond, 1978). Monrolin et al. (2018) derived a more general force-current relationship for non-uniform electrohydrodynamic geometries by expressing the volumetric Coulomb force as a surface integral. Their formulation gives:

$$F_{EHD} = \frac{D \; I}{\mu} \qquad \text{Eqn (4)}$$

where I is the total discharge current, μ is the mean ion mobility, and D is an integrated characteristic distance between the emitting and collecting electrodes. For parallel electrodes, this characteristic distance reduces to the physical electrode separation, while the general formulation allows the effective distance to depend on electrode geometry (Monrolin et al., 2018). Equation (4) therefore provides the established force-current framework used in the present model. The specific approximation used for D in the point-to-ring geometry is introduced separately in Section 2.2.

2.2. Wire-to-Ring Geometry and Space-Charge-Limited Current

To apply this analytical framework to the experimental apparatus, the point-to-ring configuration must be mapped to measurable geometric parameters. As shown in Figure 1, the emitter tip is modeled as a thin pin of radius a, the collector as a circular ring of inner radius R_c, and the axial separation distance between them along the centerline as d.

To obtain a tractable analytical baseline, the present study approximates the expanding point-to-ring drift region as an axisymmetric conical span between the emitter tip and collector perimeter. The effective geometric drift length along the hypotenuse of this span is approximated by:

$$L_{eff} = \sqrt{(R_c - a)^2 + d^2} \qquad \text{Eqn (5)}$$

Equation (5) is introduced in this study as a geometry-specific approximation of the effective distance associated with the point-to-ring configuration. It is not intended to represent a measured ion trajectory or an exact solution of the non-uniform electric field. Rather than assigning a uniform effective area to the non-uniform point-to-ring discharge, the present model adopts the geometric representation developed by Guan et al. (2018a). In their analytical treatment of a point-to-ring corona discharge, the ionization and drift regions are approximated as spherical sectors originating from the point emitter. The angular extent of this sector is determined by the axial distance between the emitter and collector and by the collector-ring radius. To close the geometry-adapted analytical model, the integrated characteristic distance appearing in Equation (4) is approximated by the geometry-specific effective distance defined in Equation

(5). Thus, for the present model, $D_{model} \approx L_{eff}$. This is a study-specific approximation and is not asserted to be the exact current-weighted distance of the physical point-to-ring discharge.

Using the notation of the present study, the limiting angle β is therefore defined geometrically as:

$$\beta = \tan^{-1}\left(\frac{R_c}{d}\right) \qquad \text{Eqn (6)}$$

where R_c is the collector-ring radius and d is the axial distance from the emitter tip to the center of the collector plane. Equivalently,

$cos(\beta) = \frac{d}{\sqrt{d^2+Rc^2}}$.

In this spherical-sector representation, current density is spatially non-uniform, and the total corona current is obtained by integrating the current flux over the spherical sector rather than by multiplying a uniform current density by an assumed lateral conical area (Guan et al., 2018a). The spherical-sector geometry is therefore used below to define a current-normal reference surface for the geometry-adapted SCL model. Guan et al.'s full point-to-ring current relation is not adopted because the corona-onset and characteristic acceleration-region parameters required by that formulation were not measured in the present experiment.

Under an ideal space-charge-limited (SCL) regime, the maximum current-density scaling between parallel boundaries is described by the Mott-Gurney relation (Mott & Gurney, 1940; Vaddi et al., 2020):

$$J_{MG} = \frac{9}{8}\varepsilon_0\mu\frac{V^2}{d^3} \qquad \text{Eqn (7)}$$

where ε_0 is the permittivity of free space, μ is the mean ion mobility, V is the applied potential difference, and d is the characteristic electrode separation. Vaddi et al. (2020) derive this expression for an idealized one-dimensional EHD drift region. Accordingly, Equation (7) is used here as an ideal SCL current-density baseline rather than as an exact description of the non-uniform point-to-ring corona discharge.

To adapt this current-density baseline to the spherical-sector geometry defined in Equation (6), a current-normal reference surface is introduced at the characteristic radial distance $r = d$. For a spherical sector with limiting angle β, its area is:

$$A_{sph} = 2\pi d^2\,(1 - \cos(\beta))$$

This reference area is a study-specific geometric closure of the model and is oriented normal to the assumed radial current flow of the spherical-sector representation. Choosing r=d also preserves the same characteristic separation used in the one-dimensional Mott-Gurney relation. The model current is therefore approximated as:

$$I_{model} = J_{MG}A_{sph}$$

This step assumes that the Mott-Gurney current-density scale can be represented by an effective mean value over the spherical-sector reference surface. It does not reproduce the full spatially varying current-density solution of Guan et al. (2018a).

Finally, applying the force-current relationship from Equation (4) with the study-specific approximation $D_{model} \approx L_{eff}$ gives:

$$F_{model} = \frac{I_{(model)} L_{eff}}{\mu}$$

Substituting Equation (7) and the spherical-sector reference area gives the closed geometry-adapted analytical model:

$$F_{model} = \frac{\frac{9\pi}{4} \varepsilon_0 V^2 L_{eff}}{d} (1 - \cos(\beta)) \qquad \text{Eqn (8)}$$

where:

$$L_{eff} = \sqrt{d^2 + (R_c - a)^2}$$

and:

$$\beta = tan^{-1} \left(\frac{R_c}{d} \right)$$

Equation (8) therefore provides an absolute idealized model-predicted thrust while retaining explicit dependence on electrode spacing, collector radius, emitter-tip radius, and applied voltage. The equation is not presented as an exact point-to-ring corona solution: it combines the established Mott-Gurney current-density scaling and EHD force-current relation with the spherical-sector geometry of Guan et al. (2018a) and the study-specific approximations defined above.

2.3. Macroscopic Momentum Transfer and Fluid Mechanics

Because the EHD device accelerates neutral ambient air via momentum collisions rather than expelling a vacuum ion beam, the macroscopic exhaust velocity measured behind the collector ring serves as a fluid-mechanical proxy for thrust. Applying standard control-volume momentum theory (White, 2015), the mass flow rate $\dot{m}$ of the neutral air passing through the effective outlet area A, as seen in Figure 2, is given by:

$$\dot{m} = \frac{\Delta m}{\Delta t} = \rho \; A \; v_{ex} \qquad \text{Eqn (9)}$$

where ρ is the neutral air density ($1.293 \; kg \; m^{-3}$ at standard atmospheric conditions) (ASHRAE, n.d.; NASA, 2021). A is the cross-sectional area of the exhaust plume, and v_{ex} is the axial exhaust velocity measured by anemometer. Because air temperature, humidity, and pressure were not recorded with sufficient precision to determine the experimental air density retrospectively, a reference dry-air density of approximately $\rho_{ref} = 1.205 \; kg \; m^{-3}$ near 20 °C and 1 atm was used in the momentum calculation. Absolute values of F_{est} therefore scale linearly with this assumed density.

Applying Newton's second law of motion to a steady one-dimensional flow stream, the momentum-based thrust estimate F generated by the device equals the time rate of change of momentum of the induced airflow (White, 2015). Under a steady one-dimensional control-volume approximation with quiescent inlet air, a representative outlet velocity, and negligible net pressure contribution across the control surface, the streamwise momentum balance gives:

$$F = \frac{\Delta p}{\Delta t} = \frac{\Delta (m \; v_{ex})}{\Delta t} = \dot{m} \; v_{ex} = \rho \; A \; {v_{ex}}^2 \qquad \text{Eqn (10)}$$

Because only a small fraction of the airflow is ionized, the ions act primarily as momentum carriers that transfer momentum to the surrounding neutral gas (Castellanos, 1998). The neutral-air density is therefore the appropriate density for the macroscopic momentum calculation. In the present experiment, the measured centerline neutral velocity is treated as representative of the downstream measurement plane, giving the simplified momentum-based thrust estimate defined in Equation (10). In a fully resolved control-volume analysis, the velocity distribution across the entire measurement plane would instead be required. The use of a single centerline velocity therefore introduces a systematic approximation.

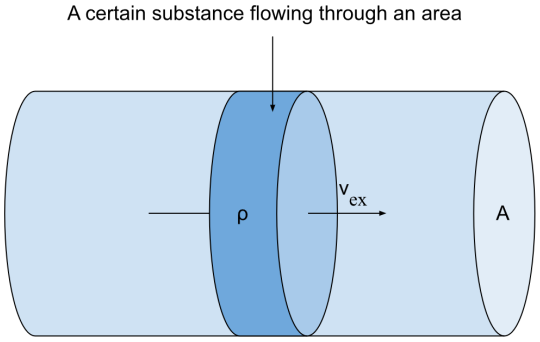

Figure 2. Schematic representation of the macroscopic control-volume mass flow rate for the induced neutral airflow. A is the effective cross-sectional outlet area, ρ is the assumed ambient neutral air density, and $v_{\mathrm{ex}}$is the axial exhaust velocity measured by the anemometer.

2.4. Thrust-to-Power Ratio and Atmospheric Regime Limitations

To evaluate whether a geometric alteration improves power-normalized performance rather than merely increasing thrust, the primary performance metric in this study is the system-level thrust-to-power ratio, defined as:

$$\eta_{EHD} = \frac{F}{P} = \frac{\rho\ A\ {v_{ex}}^2}{V\ I} \qquad \text{Eqn (11)}$$

where F is the momentum-based thrust estimate defined in Equation (10) and P is the electrical input power supplied to the high-voltage system. Combining Equation (10) with the first part of Equation (11) gives the second part of Equation (11). This system-level metric allows the tested geometries to be compared on a common power-input basis.

When comparing the experimental thrust-to-power estimates against the idealized geometry-adapted SCL model defined in Equation (8), departures between the model and experiment are expected because the analytical formulation contains both idealized transport assumptions

and simplified geometric approximations. The analytical derivation relies on several idealized assumptions: a steady, perfectly unipolar corona discharge, pure space-charge-limited current, constant ion mobility, and negligible charge loss along the drift path. The comparison model additionally applies the one-dimensional SCL current-density relation to a non-uniform point-to-ring discharge, neglects corona inception voltage in Equation (7), approximates the characteristic force distance using Equation (5), and represents the discharge geometry using the spherical-sector construction of Equation (6). The model further assumes that the Mott-Gurney current-density scale can be treated as an effective mean value over the spherical reference surface introduced in Section 2.2 and does not explicitly include aerodynamic drag.

In real atmospheric operation, however, these idealized conditions are only partially satisfied. The measured performance is actively degraded by several real-world physical phenomena documented in gas discharge literature (Raizer, 1991; Sigmond, 1978):

- Charge loss and non-ideal transport: Recombination, diffusion, ion leakage from the intended drift region, and spatial variations in charge transport can reduce the fraction of generated charge that contributes to the modeled momentum transfer.
- Fringing Fields and Radial Spread: Unlike closed duct channels, an open wire-to-ring geometry exhibits significant electrostatic fringing fields outside the primary conical volume, causing radial flow divergence that escapes axial capture.
- Unsteady electrical operation: Because the experimental high-voltage module is unregulated, variations in the discharge state can violate the steady-voltage and steady-current assumptions of the analytical model.

The analytical baseline therefore provides a reference against which the measured effects of electrode spacing and collector radius can be compared, while departures between theory and experiment can be used to examine the consequences of the model's simplifying assumptions.

3. Methodology

3.1. Experimental Framework

The investigation employed two one-factor-at-a-time (OFAT) experimental sweeps to characterize the effects of collector radius and electrode separation on the centerline velocity of the induced ionic wind. In each sweep, one geometric parameter was varied while the alternate geometric parameter, emitter geometry, electrical supply configuration, funnel geometry, and sensor position were kept unchanged. This approach allows geometry-dependent trends to be compared under a consistent apparatus configuration, while recognizing that unmonitored quantities such as the exact loaded high voltage and discharge state may also vary during operation.

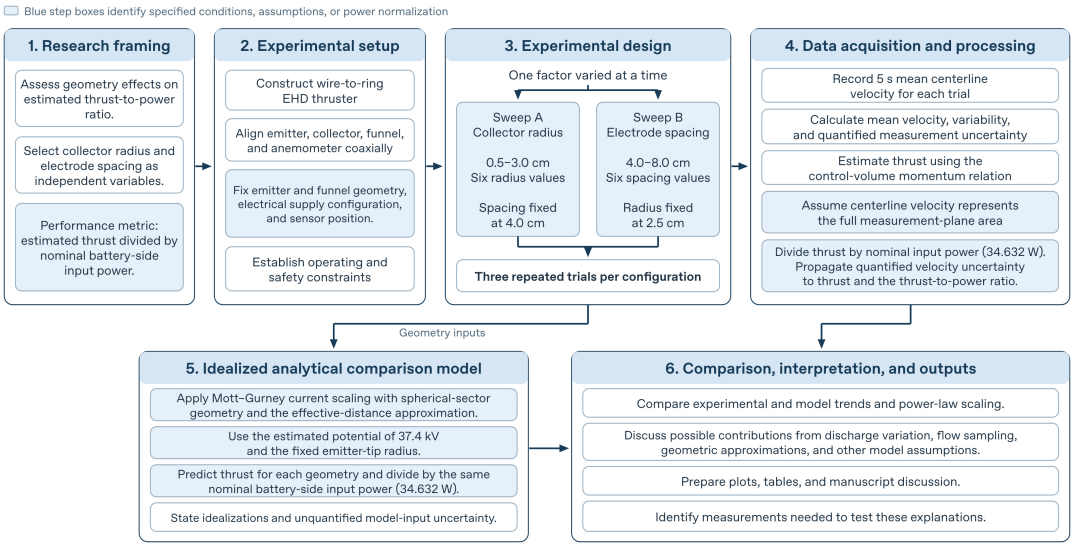

Figure 3. Overview of the integrated workflow used to evaluate geometry-dependent performance in a model electrohydrodynamic thruster.

3.2. Physical Apparatus and Flow Conditioning

The educational thruster was constructed using a simplified wire-to-ring coaxial geometry mounted on a flat, non-conductive wooden base. To prevent electrostatic leakage and parasitic grounding, all structural components such as the emitter electrode, collector ring, flow funnel, and anemometer were secured along a shared central axis using insulating supports.

The emitter electrode consisted of a rigid metallic pin with an estimated exposed-tip radius of approximately $a = 0.025$ cm. Because this microscopic dimension was derived directly from the construction geometry rather than through optical or electron microscopy characterization, it was treated throughout the investigation as an approximate, fixed structural parameter.

The collector electrodes were fabricated from bare copper wire shaped by hand into nominally circular collector rings. To evaluate the influence of radial field expansion, six interchangeable collector rings were constructed with internal radii (R_c) of 0.5 cm, 1.0 cm, 1.5 cm, 2.0 cm, 2.5 cm, and 3.0 cm.

In open-air atmospheric EHD experiments, unconfined ionic winds experience substantial radial dispersion and turbulent mixing with ambient quiescent air, which can skew axial velocity measurements (Monrolin et al., 2017). To mitigate this dispersion and ensure a controlled control-volume analysis, a non-conductive flow-conditioning funnel was positioned immediately downstream of the collector ring. The upstream opening nearest the collector had a radius of 0.5 cm, while the funnel expanded downstream to a measurement-plane radius of 5.0 cm at the anemometer. This geometry was kept unchanged for every configuration and defined the measurement-plane area used in the momentum-based thrust estimate:

$$A_{meas} = \pi(0.050)^2 = 7.854 \times 10^{-3} m^2$$

The funnel provided a consistent downstream measurement geometry but was not assumed to produce a uniform velocity profile.

3.3. Electrical Power Architecture and System Input Power

The electrical layout of the experimental apparatus is shown in Figure 4. It represents the series connection between the power supply, high-voltage generator, emitter pin, and collector

ring. High-voltage excitation was provided by an unregulated direct-current (DC) step-up boost module. The primary input of this high-voltage module was powered by a dedicated battery pack comprising two 3.7 V lithium-ion cells connected in series with a low-voltage toggle switch for operational safety.

During steady-state operation, the current supplied to the low-voltage input terminals of the DC module was measured at 4.68 A. It is critical to note that this recorded value represents the primary battery-side input current, not the secondary interelectrode corona discharge current flowing through the ionized air gap. This input current was paired with the nominal combined series voltage of the battery pack (7.4 V) to determine the total electrical input power supplied to the system ($P_{\text{sys, nom}}$):

$$P_{\text{sys,nom}} = (7.4\ \text{V})\,(4.68\ \text{A}) = 34.632\ \text{W}$$

The high-voltage output delivered across the electrodes was estimated at approximately 37.4 kV from three spark-gap breakdown estimates conducted under ambient conditions. This value was not obtained using a calibrated high-voltage probe and was not continuously monitored for each electrode geometry. It is therefore treated as a characteristic estimated interelectrode potential rather than an exact loaded operating voltage. The same electrical supply configuration was maintained throughout the geometry sweeps. Because the 37.4 kV value represents an estimated secondary high-voltage output, it was not multiplied by the measured primary battery-side input current.

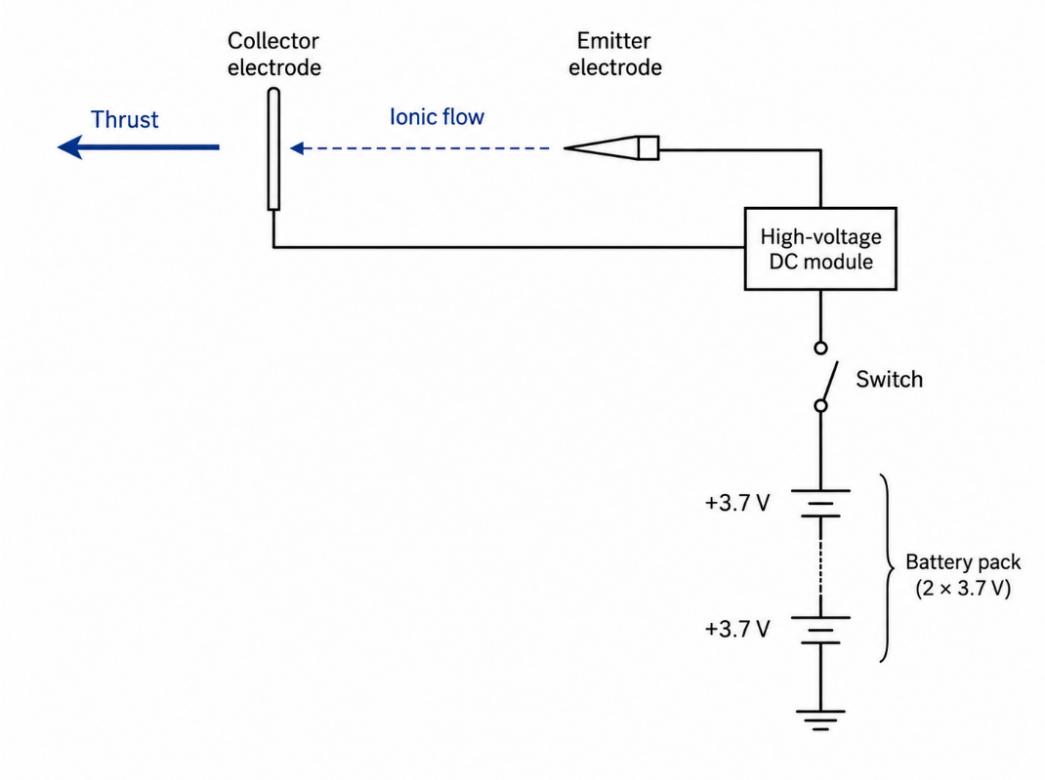

Figure 4. The electrical layout of the ionic thruster used in the experiment, including the emitter, collector, high-voltage generator, and power supply.

Furthermore, because the loaded high-voltage output and the secondary corona current were not captured simultaneously, the exact discharge-level electrical power dissipation across the air gap could not be determined retrospectively. To maintain experimental integrity and avoid introducing unverified conversion efficiencies into the performance metrics, all power-normalized

results in this study represent nominal battery-side system performance rather than isolated corona-discharge efficiency.

3.4. Experimental Design and Measurement Protocol

To systematically resolve the individual contributions of electrode separation and collector dimensions, two one-factor-at-a-time (OFAT) parametric sweeps were conducted, as summarized in Figure 3 and Table 1. For each experimental configuration, one geometric variable was manipulated across six discrete intervals while the alternate variable was held strictly constant:

- **Sweep A (Variable Collector Radius):** The axial spacing between the emitter tip and the collector ring was fixed at $d = 4.0$ cm, while the collector radius (R_c) was varied from 0.5 cm to 3.0 cm in 0.5 cm increments.
- **Sweep B (Variable Electrode Spacing):** The collector ring radius was fixed at $R_c = 2.5$ cm, while the axial electrode spacing (d) was varied from 4.0 cm to 8.0 cm across six defined intervals.

The complete operational matrix of independent geometric variables evaluated across the six trial steps is summarized in Table 1. The primary dependent variable across all trials was the macroscopic centerline exhaust velocity (v_{ex}) of the induced ionic wind. Velocity measurements were obtained using a digital vane anemometer with a stated absolute instrumental uncertainty of ± 0.005 m s^{-1}. For each individual run, the sensor head of the anemometer was aligned coaxially with the centerline of the downstream flow funnel. To account for transient airflow fluctuations and low-frequency electrostatic pulsing, the anemometer recorded the time-averaged axial velocity over a continuous five-second integration window.

Table 1. Overview of independent geometric variables evaluated across the six trial configurations

Geometric Parameters	Config1	Config2	Config 3	Config4	Config5	Config6
Collector Radius ($\mathbf{R_c}$, $\pm\mathbf{0.1}$ cm)	0.5	1.0	1.5	2.0	2.5	3.0
Electrode Spacing ($\mathbf{d}$, $\pm\mathbf{0.1}$ cm)	4.0	4.5	5.0	6.0	7.0	8.0

Each distinct geometry was evaluated using three repeated velocity measurements. The configuration with $R_c = 2.5\ cm$ and $d = 4.0\ cm$ is common to both parametric sweeps and is therefore reported in both datasets. The resulting velocity values were averaged to minimize random experimental error and statistical noise before conducting downstream aerodynamic calculations. Using the control-volume momentum relations established in Section 2.3, these time-averaged velocity measurements were converted into momentum-based thrust estimates and subsequently divided by the fixed system input power (34.632 W) to yield the experimental thrust-to-power ratio (η_{sys}) for each tested geometry.

3.5. Theoretical Baseline Computation

To establish an idealized analytical baseline against which the empirical measurements could be evaluated, model-predicted thrust was calculated for every geometry listed in Table 1 using Equation (8). Once the electrode geometry and characteristic applied voltage are specified, the model produces a deterministic prediction for each tested configuration.

For all model calculations, the emitter-tip radius was fixed at the experimentally assumed value, and the characteristic interelectrode potential was set to the estimated 37.4 kV described

in Section 3.2. Because this voltage was inferred from spark-gap behavior rather than directly measured under load for every geometry, the absolute magnitude of the model prediction should be interpreted as approximate. In particular, Equation (8) contains a V^2 dependence, making the predicted absolute thrust sensitive to uncertainty in the estimated applied voltage.

For each configuration, the effective-distance approximation was calculated as:

$$L_{eff} = \sqrt{\left(d^2 + (R_c - a)^2\right)}$$

and the spherical-sector limiting angle was calculated as:

$$\beta = \tan^{-1}\left(\frac{R_c}{d}\right)$$

These values were then substituted into the geometry-adapted thrust model:

$$F_{model} = \frac{\frac{9\pi}{4}\varepsilon_0 V^2 L_{eff}}{d}\left(1 - \cos(\beta)\right)$$

The model-predicted thrust-to-power ratio was subsequently generated by dividing the model-predicted thrust by the nominal battery-side system input power ($P = VI = 34.632$ W). These idealized model-predicted figures were generated solely to serve as a comparative baseline against the experimentally derived thrust-to-power ratios. By benchmarking the empirical data against this analytical curve, departures from the idealized model can be examined in the context of real atmospheric effects and model limitations, including charge loss, fringing fields, flow-capture limitations, and uncertainty in the effective discharge conditions.

Finally, standard uncertainty propagation was applied exclusively to the experimental data streams to account for instrument resolution and physical measurement limits. Formal uncertainty bounds were not propagated for the model-predicted values because several model inputs, particularly the estimated interelectrode voltage and emitter-tip dimension, were not characterized with sufficient measurement uncertainty for rigorous propagation. Model predictions should therefore be interpreted as idealized comparative baselines rather than precision estimates of absolute thrust. Differences between the model and experiment may reflect both these input uncertainties and systematic limitations of the analytical assumptions, including simplified geometry, non-uniform discharge behavior, aerodynamic effects, and incomplete flow capture.

4. Results and Discussion

4.1. Experimental Exhaust-Velocity measurements

Results are reported for the two controlled geometric sweeps defined in Section 3.3. The collector-radius sweep was conducted at a fixed electrode spacing of d = 4.0 cm, and the electrode-spacing sweep at a fixed collector radius of R_c = 2.5 cm. The configuration R_c = 2.5 cm with d = 4.0 cm is common to both sweeps and appears in both datasets. Experimental values carry propagated uncertainties derived from repeated velocity measurements and anemometer resolution, whereas model-predicted values are reported without uncertainty bounds. All power-normalized quantities refer to the nominal battery-side system input power of 34.632 W. That boundary encloses the battery pack and the step-up converter, so the reported η_{sys} is a system-level thrust-to-power ratio rather than an isolated corona-discharge efficiency, and it sits below what a discharge-only definition would return.

Table 2. Centerline exhaust-velocity (v_{ex}) measurements for the collector-radius sweep at a fixed electrode spacing of 4.0 cm.

Exhaust velocity (m/s)	**Collector radius** (R_c, ±0.1 cm)					
	0.5	**1.0**	**1.5**	**2.0**	**2.5**	**3.0**
Trial 1	0.00	0.07	0.21	0.42	0.56	0.68
Trial 2	0.00	0.08	0.20	0.39	0.56	0.75
Trial 3	0.00	0.07	0.19	0.38	0.55	0.74
Mean ($v_{ex} \pm u_v$)	0.000 ± 0.005	0.073 ± 0.006	0.200 ± 0.008	0.397 ± 0.013	0.557 ± 0.006	0.723 ± 0.022

Tables 2 and 3 list the three repeated centerline velocity measurements and the resulting means for each sweep. At a fixed electrode spacing of 4.0 cm, the mean exhaust velocity increased from 0.000 ± 0.005 m/s at R_c = 0.5 cm to 0.723 ± 0.022 m/s at R_c = 3.0 cm. At a fixed collector radius of 2.5 cm, the mean velocity decreased monotonically from 0.557 ± 0.006 m/s at d = 4.0 cm to 0.040 ± 0.021 m s-1 at d = 8.0 cm (Table 3). Two features of these raw data shape everything that follows. Thrust is recovered from velocity through the quadratic relation of Equation (10), so a threefold velocity change becomes an approximately ninefold thrust change, and the same squaring amplifies measurement error at the low-velocity end of both sweeps. The anemometer also sampled the centerline alone, so each tabulated value represents one point on a spreading jet rather than an area-averaged flow.

Table 3. Centerline exhaust-velocity measurements for the electrode-spacing sweep at a fixed collector radius of 2.5 cm.

Exhaust velocity (m/s)	**Electrode spacing** (d, ±0.1 cm)					
	4.0	**4.5**	**5.0**	**6.0**	**7.0**	**8.0**
Trial 1	0.56	0.36	0.28	0.25	0.10	0.07
Trial 2	0.56	0.38	0.29	0.21	0.11	0.00
Trial 3	0.55	0.37	0.28	0.20	0.10	0.05
Mean ($v_{ex} \pm u_v$)	0.557 ± 0.006	0.370 ± 0.008	0.283 ± 0.006	0.220 ± 0.016	0.103 ± 0.006	0.040 ± 0.021

4.2. Representative Performance Calculation and Uncertainty

For each geometric configuration, the three repeated centerline velocity measurements were first averaged. The spread between repeats was represented by the sample standard deviation:

$$s = \sqrt{\left(\frac{\Sigma_{i=1}^{n} \left(v_i - \bar{v} \right)^2}{n-1} \right)}$$

The random uncertainty of the mean was then estimated using the standard error:

$$u_{rand} = \frac{s}{\sqrt{n}}$$

where n=3. This was combined in quadrature with the stated instrumental uncertainty of the

anemometer, $u_{inst} = 0.005\ m\ s^{-1}$:

$$u_{\bar{v}} = \sqrt{(u_{rand}^2 + u_{inst}^2)}$$

As an example, for R_c=3.0 cm and d=4.0 cm, the measured velocities were 0.68, 0.75, and 0.74 $m\ s^{-1}$. These give:

$$\bar{v} = 0.723\ m\ s^{-1}$$

$$s = 0.0379\ m\ s^{-1}$$

$$u_{rand} = 0.0219\ m\ s^{-1}$$

and therefore:

$$u_{\bar{v}} = 0.0224\ m\ s^{-1}$$

giving a reported centerline velocity of:

$$\bar{v} = 0.723 \pm 0.022\ m\ s^{-1}$$

The measured centerline velocity was then converted into a simplified momentum-based thrust estimate. The downstream measurement-plane radius was 5.0 cm, corresponding to:

$$A_{meas} = \pi(0.050)^2 = 7.854 \times 10^{-3}\ m^2$$

Using the assumed reference air density $\rho = 1.205\ kg\ m^{-3}$, the thrust estimate was calculated as:

$$F_{est} = \rho\ A_{meas}\bar{v}^2$$

This relation treats the measured centerline velocity as representative of the full measurement area. It therefore provides a momentum-equivalent thrust estimate rather than a direct thrust measurement. The uncertainty reported for F_{est} reflects the propagated velocity uncertainty only; systematic uncertainty associated with the assumed air density, measurement area, and use of a single centerline velocity was not sufficiently characterized for formal propagation.

For the regular measurement points, first-order uncertainty propagation gives:

$$u_F = 2\rho\ A_{meas}\bar{v}\ u_{\bar{v}}$$

For the example configuration:

$$F_{est} = 4.95\ mN$$

and:

$$u_F = 0.31\ mN$$

giving:

$$F_{est} = 4.95 \pm 0.31 \ mN$$

The nominal battery-side system input power was calculated from the nominal series battery voltage and measured battery-side operating current:

$$P_{sys,nom} = V_{bat,nom} \ I_{bat}$$

$$P_{sys,nom} = (7.4 \ V)(4.68 \ A) = 34.632 \ W$$

No formal uncertainty was assigned to $P_{sys,nom}$ because the loaded battery voltage and measurement uncertainty of the battery-side current were not recorded in sufficient detail for retrospective propagation. The value is therefore used as a fixed nominal system-power reference rather than a precision measurement of discharge power.

The system-level thrust-to-power ratio was calculated as:

$$\eta_{sys} = \frac{F_{est}}{P_{sys,nom}}$$

and the displayed experimental uncertainty was obtained from the velocity-derived thrust uncertainty:

$$u_{\eta} = \frac{u_F}{P_{sys,nom}}$$

For the example configuration, this gives:

$$\eta_{sys} = 143.0 \pm 8.9 \ mN \ kW^{-1}$$

4.3. Collector-Radius Dependence

Table 4 presents the collector-radius sweep. The measured system thrust-to-power ratio increased from 1.47 ± 0.24 mN kW^{-1} at R_c = 1.0 cm to 142.98 ± 8.86 mN kW^{-1} at R_c = 3.0 cm, an increase of roughly two orders of magnitude across a threefold change in radius, with no downstream airflow resolved at R_c=0.5 cm. Model-predicted values rose over the same interval from 19.7 to 630.1 mN kW^{-1}. The model exceeds the experiment at every detected configuration, but the size of that excess is not fixed. The ratio of predicted to measured performance falls from approximately 52.9 at R_c = 1.0 cm, through 15.7, 6.9, and 5.3, to 4.4 at 3.0 cm. Agreement therefore improves as the collector widens, which indicates that the discrepancy is geometry-dependent rather than a constant calibration offset.

Table 4. Experimental and idealized model-predicted thrust-to-power ratios for the collector-radius sweep at a fixed electrode spacing of 4.0 cm.

Quantity	**Collector radius** (R_c, ±0.1 cm)					
	0.5	**1.0**	**1.5**	**2.0**	**2.5**	**3.0**
η_{sys} (mN kW^{-1})	ND	1.47 ± 0.24	10.93 ± 0.83	43.00 ± 2.82	84.68 ± 1.83	142.98 ± 8.86
η_{model} (mN kW^{-1})	19.7	77.7	171.5	297.6	451.8	630.1

Figure 5 shows the measured radius data with propagated uncertainty. The detected configurations were well described by the power-law relationship$\eta_{sys} = 1.7585 R_c^{4.2130}$, with $R^2 = 0.9870$. A positive exponent means the dependent variable rises with the independent variable, and because the fitted exponent exceeds unity, the rate of increase itself grows across the tested range. The relatively high coefficient of determination indicates that a power curve describes the pattern well, though R^2 alone does not establish a power law as the governing mechanism. A larger collector alters both the electric-field distribution and the region through which charge and induced airflow develop, and it also presents a larger aperture to the spreading jet, so a greater fraction of the induced flow may reach the measurement plane. These effects are not separated here, because field distribution, corona current, and the full velocity field were not measured independently. The error bars shown reflect repeat-to-repeat variation and instrumental resolution only; the systematic contributions just described could not be assigned numerical values from the available measurements.

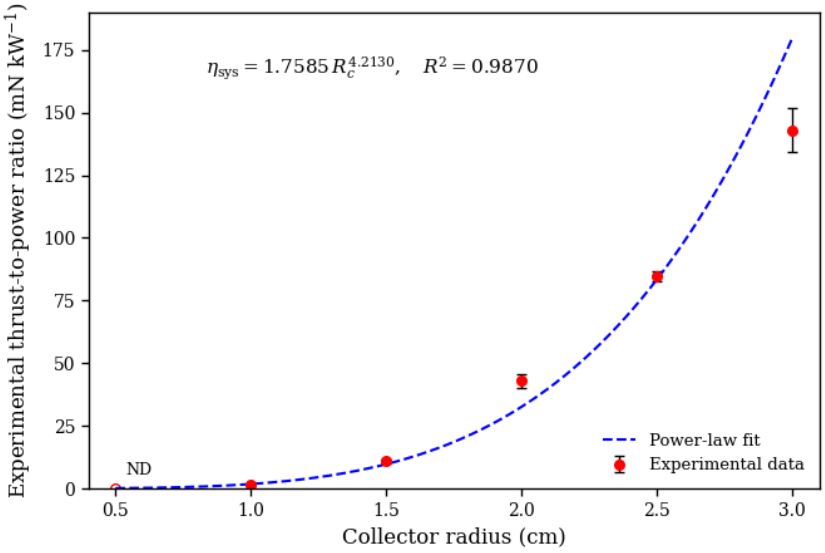

Figure 5. Experimental system thrust-to-power ratio as a function of collector radius at a fixed electrode spacing of 4.0 cm. Error bars show propagated uncertainty from repeated velocity measurements and anemometer uncertainty. The 0.5 cm configuration produced no detected downstream airflow and was excluded from the power-law regression.

Figure 6 shows the corresponding analytical prediction, which reproduced the direction of the measured trend. Predicted thrust-to-power rose from 19.66 mN kW^{-1} at R_c = 0.5 cm to 630.07 mN kW^{-1} at 3.0 cm, with absolute predicted thrust increasing from 0.681 to 21.820 mN and followed $\eta_{model} = 76.6951 \times R_c^{1.9385}$, with $R^2 = 0.9998$. Near-unity correlation is expected for

a deterministic expression evaluated across a smooth geometric sweep and indicates only that a power law describes the calculated points closely. It carries no information about physical accuracy. The measured exponent of approximately 4.21 is more than twice the predicted 1.94. The vertical position of the model curve is additionally sensitive to the 37.4 kV estimate, since Equation (8) scales with V^2, so the absolute offset in Table 4 should be weighted less heavily than the difference in slope.

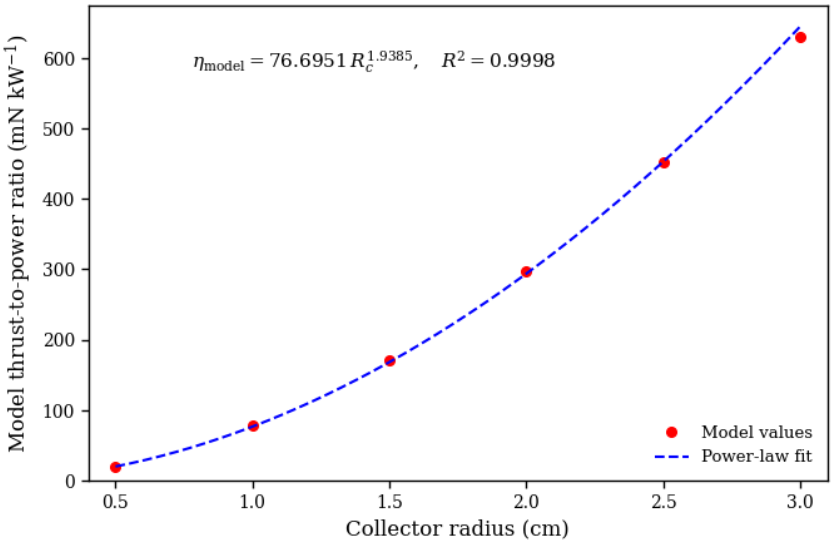

Figure 6. Idealized model-predicted thrust-to-power ratio as a function of collector radius at a fixed electrode spacing of 4.0 cm.

4.4. Electrode-Spacing Dependence

Table 5 reports the electrode-spacing sweep, in which measured performance fell at every tested increase in separation, from 84.68 ± 1.83 mN kW^{-1} at d = 4.0 cm to 0.44 ± 0.47 mN kW^{-1} at 8.0 cm. Model-predicted values also decreased, but far more gently, from 451.8 to 120.4 mN kW^{-1}. Here the ratio of predicted to measured performance moves in the opposite direction to the radius sweep, rising from approximately 5.3 at 4.0 cm, through 9.7, 13.6, and 15.9, to 53.5 at 7.0 cm and roughly 274 at 8.0 cm. Model and experiment therefore converge as the collector widens and diverge sharply as the electrodes separate.

Table 5. Experimental and idealized model-predicted thrust-to-power ratios for the electrode-spacing sweep at a fixed collector radius of 2.5 cm.

Quantity	**Electrode spacing** (d, ±0.1 cm)					
	4.0	**4.5**	**5.0**	**6.0**	**7.0**	**8.0**
η_{sys} (mN kW^{-1})	84.68± 1.83	37.41 ± 1.54	21.94 ± 0.93	13.23 ± 1.93	2.92 ± 0.34	0.44 ± 0.47*
η_{model} (mN kW^{-1})	451.8	363.0	297.8	210.3	156.2	120.4

Figure 7 presents the measured spacing data. Six-point regression gave:

$$\eta_{sys} = 1.5632 \times 10^6 \; d^{-6.9399}, \; R^2 = 0.9354$$

A negative exponent describes an inverse relationship, and its large magnitude indicates a steep response over the tested interval. The final configuration requires additional care, because its propagated uncertainty is comparable to the calculated value. Recalculating without that point gives $\eta_{sys} = 1.7155 \times 10^5 \ d^{-5.5188}$, $R^2 = 0.9593$, so the fitted exponent shifts by more than 1.4 when a single measurement is removed. Both regressions support the same conclusion, and reporting the sensitivity is preferable to reporting one exponent, since a regression coefficient can appear mathematically precise even when the measurements do not justify treating every digit as exact. The centerline sampling limitation is most consequential at this end of the sweep. Point-to-ring EHD flow measurements show that downstream velocity peaks near the axis and falls with radial distance (Guan et al., 2018b), and as the jet weakens and spreads at larger spacings, a fixed centerline probe captures a progressively less representative sample of an already small flow. Because thrust scales with velocity squared, that sampling bias enters the estimate quadratically.

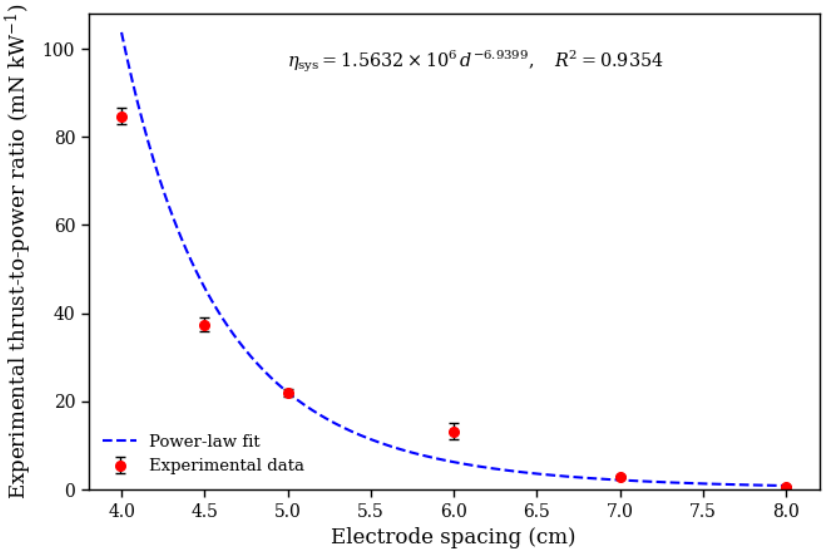

Figure 7. Experimental system thrust-to-power ratio as a function of electrode spacing at a fixed collector radius of 2.5 cm. Error bars show propagated measurement uncertainty. The 8.0 cm configuration is close to the measurement detection limit.

Figure 8 shows that the analytical model again predicted the correct direction. Predicted thrust-to-power fell from 451.84 mN kW^{-1} at 4.0 cm to 120.45 mN kW^{-1} at 8.0 cm, with absolute predicted thrust decreasing from 15.648 to 4.171 mN, following $\eta_{model} = 6401.0319 \ d^{-1.9085}$, $R^2 = 0.9999$. The predicted exponent of approximately -1.91 is far shallower than the measured -6.94, or -5.52 with the near-detection-limit point excluded. Even the more conservative experimental figure is roughly three times the predicted magnitude.

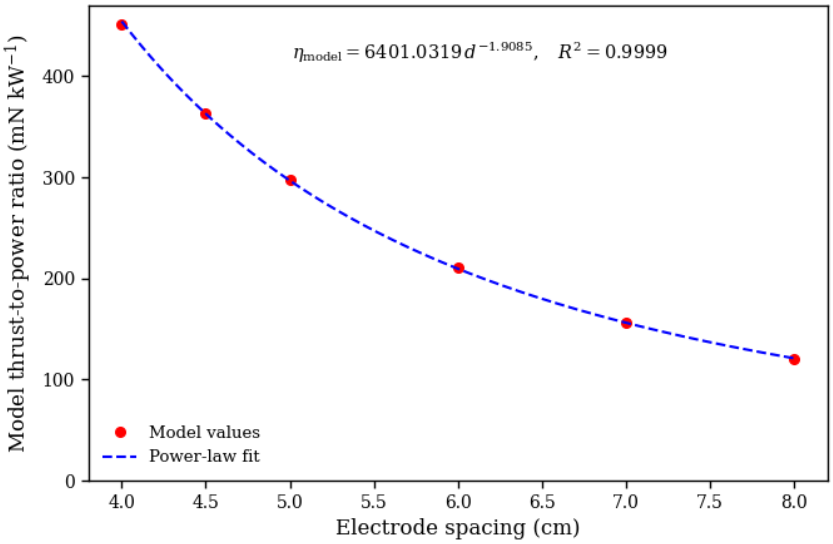

Figure 8. Idealized model-predicted thrust-to-power ratio as a function of electrode spacing at a fixed collector radius of 2.5 cm.

4.5. Experimental-Model Comparison and Limitations

Table 6 consolidates the four power-law relationships. Experiment and model agree on sign for both geometric variables and disagree on magnitude by approximately a factor of two in the radius exponent and a factor of three in the spacing exponent. This distinction matters when a model is assessed against data. Predicting the correct direction of a trend is weaker evidence than predicting both its direction and its rate of change, and the analytical formulation succeeds at the first while failing at the second. The fitted exponents describe the behavior of these datasets over the tested ranges and are not presented as universal scaling laws.

Table 6. Power-law relationships obtained from the experimental and idealized model-predicted thrust-to-power datasets.

Dataset	Independent variable	Power-law relationship	R^2
Experimental	Collector radius	$\eta_{sys} \propto R_c^{4.21}$	0.987
Experimental	Electrode spacing	$\eta_{sys} \propto d^{-6.94}$	0.935
Experimental (excluding 8.0 cm)	Electrode spacing	$\eta_{sys} \propto d^{-5.52}$	0.959
Theoretical	Collector radius	$\eta_{model} \propto R_c^{1.94}$	0.9998
Theoretical	Electrode spacing	$\eta_{model} \propto d^{-1.91}$	0.9999

The opposing behavior of the two over-prediction ratios points toward a specific origin for the disagreement. The analytical model assumes space-charge-limited current, constant ion mobility, negligible charge loss, and a fixed applied potential, and it neglects both corona inception voltage and aerodynamic drag. Under a fixed unregulated supply, increasing electrode separation lowers the mean interelectrode field and moves the discharge toward corona onset, so the actual current is expected to fall faster with spacing than the space-charge-limited relation allows. Widening the collector at fixed spacing does not impose the same penalty and may improve capture of the induced flow. A model that assumes a geometry-independent discharge would therefore diverge from measurement as spacing grows and converge as radius grows, which is the pattern observed in Tables 4 and 5. This interpretation is consistent with the data but not established by them, since corona current was not measured. Thrust was likewise inferred from velocity

rather than measured with a micro-newton balance, so the momentum-based estimates lack an independent mechanical check.

This investigation targets atmospheric electrohydrodynamic thrust generation using accessible construction methods and commercially available high-voltage equipment. The results are consequently most useful as a controlled comparison of geometric effects within one apparatus rather than as absolute performance limits for EHD propulsion in general. The educational value comes from connecting several layers of physics inside a single system. The anemometer supplies a directly observed quantity, neutral-air velocity. Control-volume momentum theory converts that observation into an estimated force. Electrical input power permits normalization to a system-level metric. An idealized EHD model then predicts how geometry should influence the device. The disagreement between these stages demonstrates why a mathematically consistent model can still diverge from a physical experiment when its assumptions do not describe every part of the real system.

Future work should focus on measurements that separate the contributing effects. Recording loaded high voltage and corona current independently at every configuration would test the discharge-strength interpretation advanced above. A multi-point downstream velocity profile would test whether centerline velocity represents the full measurement plane, particularly at large spacings where the sampling bias is expected to be largest. Direct thrust measurement with a micro-newton balance would provide an independent check on the momentum-based estimate. Together these three measurements would determine whether the stronger experimental geometry dependence originates in the electrical discharge, in the downstream airflow, or in a combination of both.

At very low measured velocities, linear uncertainty propagation through the quadratic thrust relation becomes less reliable. In particular, the d=8.0 cm result has an uncertainty comparable to its mean velocity, while all three measurements at $R_c = 0.5$ cm were zero. The former is therefore treated as a near-detection-limit result, while the latter is reported as **no downstream airflow detected above the instrumental resolution**, rather than as evidence of exactly zero thrust.

Power-law relationships were obtained by ordinary least-squares regression after logarithmic transformation of independent and dependent variables. Propagated experimental uncertainties were displayed as error bars but were not used as regression weights. The reported R^2 values refer to the log-transformed regressions. Because a logarithmic fit cannot include a zero value, the no-detection collector-radius configuration was excluded from the radius regression.

5. Conclusion

This study investigated how collector radius and electrode spacing affect the system-level thrust-to-power performance of a simplified wire-to-ring atmospheric EHD thruster. Both geometric variables produced clear trends. Increasing collector radius increased measured performance, while increasing electrode spacing produced a strong decrease.

At a fixed electrode spacing of 4.0 cm, no downstream airflow was detected above the instrumental resolution for the 0.5 cm collector. Across the detected radius range from 1.0 to 3.0 cm, the measured system thrust-to-power ratio increased from 1.47 ± 0.24 to 142.98 ± 8.86 mN kW^{-1}. The corresponding experimental power-law exponent was approximately 4.21. At a fixed collector radius of 2.5 cm, increasing electrode spacing from 4.0 to 8.0 cm reduced the measured ratio from 84.68 ± 1.83 to 0.44 ± 0.47 mN kW^{-1}. Because the final spacing measurement was close to the detection limit, the fitted experimental spacing exponent ranged from approximately -5.52 to -6.94 depending on whether this configuration was included.

The idealized geometry-adapted analytical model reproduced the direction of both geometric

trends but predicted weaker scaling. Its fitted exponents were approximately 1.94 for collector radius and -1.91 for electrode spacing. The model also predicted higher absolute performance than the experiment. It therefore provides a useful analytical baseline for geometric behavior, but it does not reproduce the complete response of the physical apparatus.

The main limitation of the experimental thrust estimate is that one centerline velocity measurement was treated as representative of the full downstream measurement area. The reported error bars describe the quantified velocity uncertainty, while systematic effects such as the unknown velocity profile, estimated high voltage, hand-built electrode geometry, and unmeasured corona current could not all be assigned numerical uncertainties. The thrust-to-power ratio also refers to nominal battery-side system power rather than isolated corona-discharge power.

These limitations are themselves relevant to the educational aim of the investigation. The experiment provides a progression from direct measurement, to derived thrust, to system-level performance, to analytical prediction, and finally to evaluating the assumptions that separate a model from a real device. In this way, a relatively accessible EHD apparatus can be used to study electrostatics, ion transport, momentum transfer, regression, experimental uncertainty, and model limitations within one quantitative investigation.

A stronger continuation of this work would directly measure loaded high voltage and corona current for each geometry, obtain a spatial velocity profile rather than a single centerline measurement, and independently measure mechanical thrust. These measurements would help determine whether the stronger experimental geometry dependence originates mainly from changes in the electrical discharge, the downstream airflow, or a combination of both.

6. References

ASHRAE. (n.d.). *Standard air*. In *ASHRAE Terminology*. https://terminology.ashrae.org/?entry=standard+air

Belan, M., Arosti, L., Polatti, R., Maggi, F., Fiorini, S., & Sottovia, F. (2021). A parametric study of electrodes geometries for atmospheric electrohydrodynamic propulsion. *Journal of Electrostatics, 113*, 103616. https://doi.org/10.1016/j.elstat.2021.103616

Belan, M., Terenzi, R., Trovato, S., & Usuelli, D. (2022). Effects of the emitters density on the performance of an atmospheric ionic thruster. *Journal of Electrostatics, 120*, 103767. https://doi.org/10.1016/j.elstat.2022.103767

Burghard, B. L., Holsboer, D. J., & Schrama, V. R. (2023). *Unlocking ionic thrust: The power of electrode geometry*. Rijnlands Lyceum Sassenheim. https://storage.knaw.nl/2024-05/pws%20unlocking%20ionic%20thrust%20bramburghard-saj-burghard-holsboer-schrama.pdf

Castellanos, A. (Ed.). (1998). *Electrohydrodynamics* (CISM International Centre for Mechanical Sciences, Vol. 380). Springer. https://doi.org/10.1007/978-3-7091-2522-9

Cattani, M., Vannucci, A., & Souza, V. G. (2015). Lifter: High voltage plasma levitation device. *Revista Brasileira de Ensino de Física, 37*(3), 3307. https://doi.org/10.1590/S1806-11173731869

Gadisa, D., & Bang, H. (2023). *Modeling and parametric performance analysis of field emission electric propulsion* [Preprint]. Research Square. https://doi.org/10.21203/rs.3.rs-3158803/v1

Gökmen, S. Z. (2025). *Power-to-thrust analysis: Investigating feasibility of ionic thruster performance for space launch* [Preprint]. engrXiv. https://doi.org/10.31224/5626

Gu, L., Tan, W., He, J., Jiang, Z., Chen, X., Ren, W., & Jin, Z. (2023). Relationship between corona discharge thrust and applied voltage's polarity. *Energies, 16*(14), 5257. https://doi.org/10.3390/en16145257

Guan, Y., Vaddi, R. S., Aliseda, A., & Novosselov, I. (2018a). Analytical model of electro-hydrodynamic flow in corona discharge. *Physics of Plasmas, 25*(8), 083507. https://doi.org/10.1063/1.5029403

Guan, Y., Vaddi, R. S., Aliseda, A., & Novosselov, I. (2018b). Experimental and numerical investigation of electrohydrodynamic flow in a point-to-ring corona discharge. *Physical Review Fluids, 3*(4), 043701. https://doi.org/10.1103/PhysRevFluids.3.043701

Hart, F. X., & Massey, J. S. (1981). Two electrohydrodynamic demonstrations. *American Journal of Physics, 49*(7), 695–696. https://doi.org/10.1119/1.12433

Hou, M., Zhang, J., & Quan, R. (2025). Sawtooth multi-ring electrodes for ionic wind propulsion. *Scientific Reports, 15*, 17471. https://doi.org/10.1038/s41598-025-02775-5

Iranshahi, K., Defraeye, T., Rossi, R. M., & Müller, U. C. (2024). Electrohydrodynamics and its applications: Recent advances and future perspectives. *International Journal of Heat and Mass Transfer, 232*, 125895. https://doi.org/10.1016/j.ijheatmasstransfer.2024.125895

Kahol, O., Belan, M., Pacchiani, M., & Montenero, D. (2023). Scaling relations for the geometry of wire-to-airfoil atmospheric ionic thrusters. *Journal of Electrostatics, 123*, 103815. https://doi.org/10.1016/j.elstat.2023.103815

Kuhnen, C. A., Isoppo, E. A., & Ouriques, G. R. (2007). Forças em capacitores assimétricos submetidos a altas tensões. *Revista Brasileira de Ensino de Física, 29*(2), 231–239. https://doi.org/10.1590/S0102-47442007000200008

MIT Space Propulsion Laboratory. (n.d.). *What is electric propulsion?* https://spacepropulsion.mit.edu/electric-propulsion/

Monrolin, N., Plouraboué, F., & Praud, O. (2017). Electrohydrodynamic thrust for in-atmosphere propulsion. *AIAA Journal, 55*(12), 4296–4305. https://doi.org/10.2514/1.J055928

Monrolin, N., Praud, O., & Plouraboué, F. (2018). Electrohydrodynamic ionic wind, force field, and ionic mobility in a positive DC wire-to-cylinders corona discharge in air. *Physical Review Fluids, 3*(6), 063701. https://doi.org/10.1103/PhysRevFluids.3.063701

Mott, N. F., & Gurney, R. W. (1940). *Electronic processes in ionic crystals*. Clarendon Press.

National Aeronautics and Space Administration. (2015). *NASA facts: Ion propulsion* [Fact sheet]. https://www.nasa.gov/wp-content/uploads/2015/08/ionpropfact_sheet_ps-01628.pdf

National Aeronautics and Space Administration. (2021, May 7). *Mass flow rate*. Glenn Research Center. https://www.grc.nasa.gov/www/BGH/mflow.html

National Aeronautics and Space Administration. (2024). *State of the art small spacecraft technology: 4.0 In-space propulsion*. https://www.nasa.gov/wp-content/uploads/2025/02/soa-2024.pdf

National Aeronautics and Space Administration. (n.d.). *Chemical propulsion systems*. Glenn Research Center. https://www1.grc.nasa.gov/research-and-engineering/chemical-propulsion-systems/

Przeniczny, Z. (1972). A variation of electric wind experiment. *The Physics Teacher, 10*(6), 338.

Raizer, Y. P. (1991). *Gas discharge physics*. Springer. https://doi.org/10.1007/978-3-642-61247-3

Sigmond, R. S. (1978). Corona discharges. In J. M. Meek & J. D. Craggs (Eds.), *Electrical breakdown of gases* (pp. 319–384). Wiley.

Terenzi, R., Trovato, S., Usuelli, D., & Belan, M. (2025). Atmospheric electroaerodynamic thrusters with grid collectors. *Scientific Reports, 15*, 41513. https://doi.org/10.1038/s41598-025-25308-6

Vaddi, R. S., Guan, Y., Mamishev, A., & Novosselov, I. (2020). Analytical model for electrohydrodynamic thrust. *Proceedings of the Royal Society A: Mathematical, Physical and Engineering Sciences, 476*(2241), 20200220. https://doi.org/10.1098/rspa.2020.0220

White, F. M. (2015). *Fluid mechanics* (8th ed.). McGraw-Hill Education.